

ARTICLE OPEN



Accelerated sulfate reducing bacteria corrosion of X80 pipeline steel welded joints under organic carbon source starvation

Qin Wang¹, Xiaobao Zhou¹, Hui Su¹, Minghua Zhang¹, Zhi Li¹ and Tangqing Wu¹✉

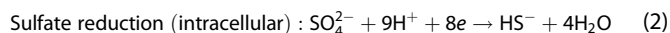
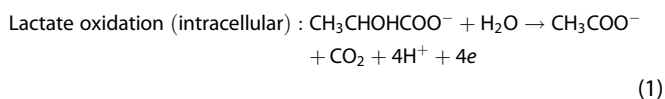
Sulfate-reducing bacteria (SRB) corrosion of X80 steel welded joint under organic carbon source starvation was investigated in the paper. The results showed that the number of planktonic cells is much less than that of sessile cells after 720 h immersion. The number of sessile cells in the base metal (BM) in the medium with 1% carbon source is the largest. Starving SRB cells accelerated simultaneously the uniform corrosion and localized corrosion of the welded joints, and the acceleration effect on the latter was much higher than that of the former. In all mediums, the density and average depth of pits in the BM and weld zone (WZ) were much larger than those in the heat affected zone (HAZ). SRB corrosion of the welded joint was strongly selective, and organic carbon source starvation further enhanced the selectivity.

npj Materials Degradation (2022)6:82; <https://doi.org/10.1038/s41529-022-00291-9>

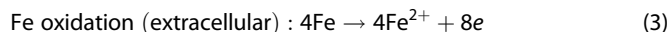
INTRODUCTION

Long-distance pipelines, which permanently served in complex soil environments, are the main transportation channels for oil and natural gas¹. Corrosion failure of pipeline steel is one of the important threats to the safe operation of long-distance pipelines^{2,3}. It was reported that more than 20% of pipeline system failures were caused by microbiologically influenced corrosion (MIC)^{4–7}. MIC is the corrosion processes of metals enhanced by the synergistic interaction of microorganisms, biofilms and metabolic products^{8–10}. The soil environment that the pipeline steel served in is usually anaerobic or hypoxic, which provides necessary conditions for the survival of anaerobic sulfate-reducing bacteria (SRB)^{11,12}. Therefore, SRB corrosion has become the main MIC type of pipeline steel, and has received extensive attention from scholars and engineers throughout the world^{13–15}.

In environments with abundant organic carbon sources, SRB can obtain electrons by lactate oxidation to complete the sulfate reduction as follows^{16,17}:



However, organic carbon sources are always scarce under mature biofilm and it is difficult for SRB cells in it to obtain the organic carbon source from the medium^{18,19}. Thus, these SRB cells turn to obtaining energy through the reduction of intracellular sulfate (Reaction (2)) and the oxidation of extracellular iron (Reaction (3))²⁰.



This process requires the extracellular electrons to transfer cross the cytomembrane. The electron transfer from the outside to inside of the cell can be achieved directly by the redox proteins (c-type cytochromes, conductive nanowires) on the bacteria surface, or indirectly under the help of electron carriers^{21–23}.

SRB utilizes electrons donated by the iron matrix to reduce sulfate to sulfide and obtain the required energy^{24,25}.

It can be clearly seen from the reactions (2) and (3) that the iron matrix acts as an electron donor under mature biofilm, inducing corrosion of the iron matrix²⁶. This is the extracellular electron transfer (EET) mechanism of SRB corrosion for carbon steel²⁷. Besides, it was reported that SRB become more aggressive under organic carbon source starvation, accelerating the corrosion of carbon steels. Xu et al.¹⁶ confirmed that the SRB corrosion rate of C1018 carbon steel was accelerated and the depth of corrosion pits on the steel surface was increased in organic carbon source starvation medium. Pre-established SRB biofilms on carbon steel become more corrosive under organic carbon source starvation. Li et al.²⁸ also obtained similar results through organic carbon source starvation experiments, and confirmed that SRB uses L245 carbon steel as an electron donor to maintain metabolism under starvation conditions. Dou et al.²⁹ compared carbon steel SRB corrosion in standard medium and under organic carbon starvation conditions. The results showed that the weight loss of carbon steel was the highest (6.6 mg cm⁻²) under the level of 20% carbon source, while the weight loss of carbon steel in the standard medium was the lowest (3.3 mg cm⁻²).

On the other hand, MIC of welded joints has also attracted the increasing attention throughout the world. Nandakumar et al.³⁰ studied the corrosion of AISI 304 L-type stainless steel by *Pseudomonas sp.*. It was found that the weld zone (WZ) with many grains and grain boundaries showed more bacterial attachment, while the base metal (BM) had the least number of bacteria. Therefore, changes in the micro-structure after welding can affect bacterial attachment, resulting in selective corrosion of welded joints. Zhu³¹ studied the SRB corrosion of manual TIG welded joints of X80 steel in artificial seawater and verified that the most serious selective corrosion occurred in the WZ. Recently, we investigated the SRB corrosion behavior of X80 pipeline steel welded joints and found that SRB tended to adhere to the BM and WZ, and accelerate the localized corrosion process in these two zones. However, SRB did not like to adhere to the heat affected zone (HAZ) surface, reducing the SRB corrosion tendency in the HAZ³². Obviously, SRB corrosion of different zones of

¹School of Materials Science and Engineering, Xiangtan University, Xiangtan 411105, China. ✉email: tqwu10s@alum.imr.ac.cn

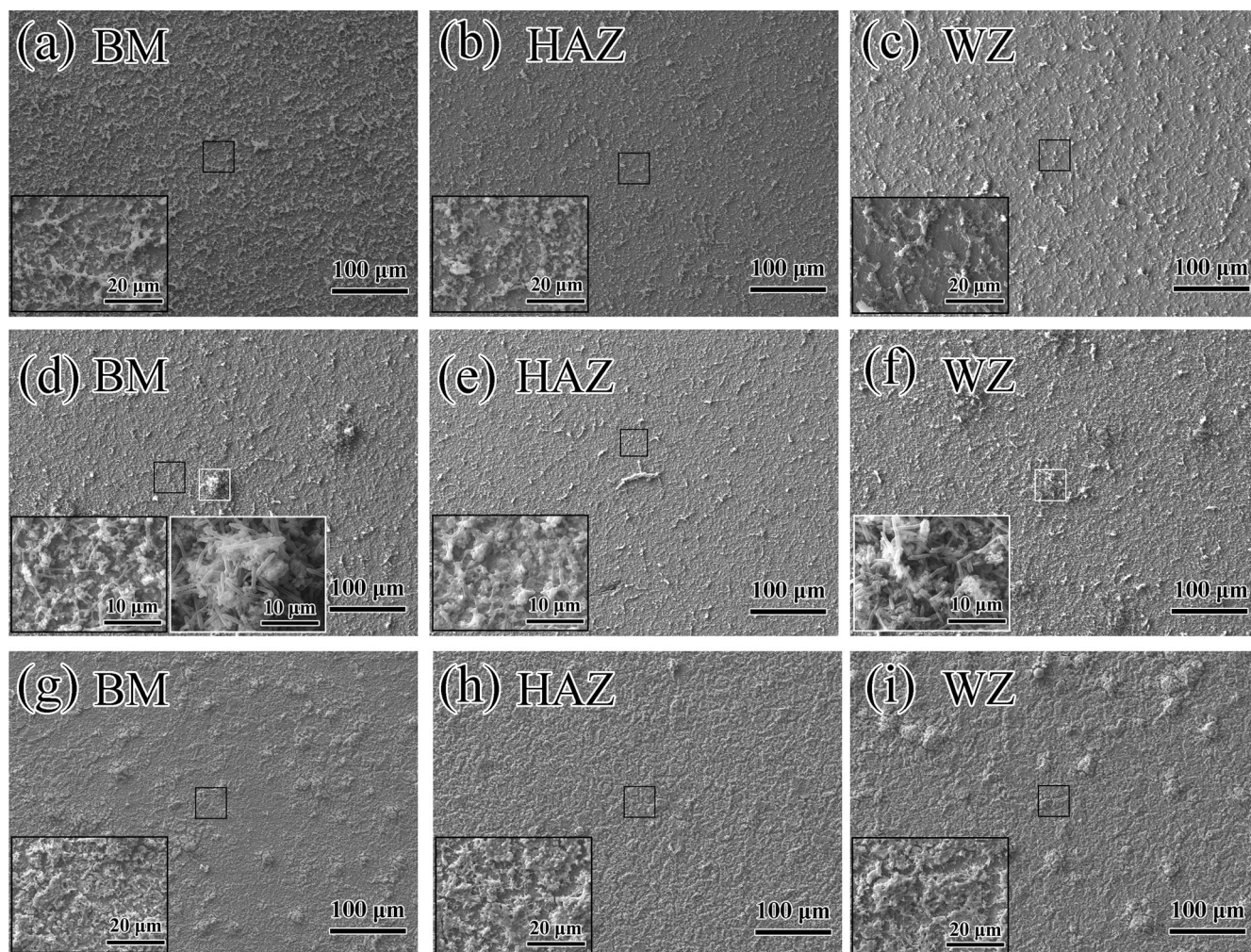


Fig. 1 Biofilm on the surface of the welded joint. **a–c** Show biofilm morphology on different zones after 3 d pre-incubation. **d–f** Show biofilm morphology on different zones after 7 d pre-incubation. **g–i** Show biofilm morphology on different zones after 14 d pre-incubation.

carbon steel welded joints is quite different from each other. Unfortunately, the study and exploration on the related mechanism are still not enough, thus it certainly looks worthy of further investigation.

From the above, EET is the main corrosion mechanism of carbon steel under the action of SRB metabolism. In the organic carbon source starvation environment, SRB use carbon steel as an electron donor and accelerate its corrosion process. Besides, the micro-structure and electrochemical activity of different zones of welded joints are significantly different, which affects the microbe adhesion and the electron transfer. Therefore, two questions emerge: When carbon-starved SRB encounter a welded joint, do they use all zones or a specific zone of the welded joint as electron donor(s)? What is the difference in corrosion behavior between the selected electron donor zone and other zones of the welded joints under organic carbon source starvation condition? These questions are very interesting, and they also are important for in-depth understanding of the SRB corrosion mechanism of metals. However, to our knowledge, they are still unknown. To discover the answers of these questions, the SRB corrosion of an X80 steel welded joint under organic carbon source starvation conditions was studied in this work. The results of the work are beneficial for us to reveal the behavior and mechanism of SRB corrosion for carbon steel welded joints.

RESULTS

Mature biofilms on the sample surface after pre-incubation

The biofilm morphology on different zones of the welded joint after 3 d, 7 d, and 14 d pre-incubation in the medium with 100% carbon source containing SRB are shown in Fig. 1. After 3 d pre-incubation, thin layer of mature biofilms were respectively attached on the three zones of the sample surfaces, and the threadlike SRB were inlaid on the sample surfaces to form a loose network of biofilms. Obviously, no microbial tubercles formed on the three zones and the difference between them was very slight. After 7 d pre-incubation, the biofilm on the three zones became markedly different. Cluster-like microbial tubercles containing a large number of SRB and flocculent corrosion products appeared on the BM and WZ zones of the welded joint. However, after 14 d pre-incubation, the number of microbial tubercles on the BM and WZ zones continued to increase. According to our previous study, localized corrosion rightly generated under the microbial tubercles³². Therefore, the mature biofilms after 3 d pre-incubation in the medium with 100% carbon source containing SRB were selected as the original biofilms for the organic carbon source starvation experiment in this work.

Planktonic, sessile cell counts and corrosion rates

The number of planktonic cells in the mediums with different carbon source levels are shown in Fig. 2a. Three similar typical

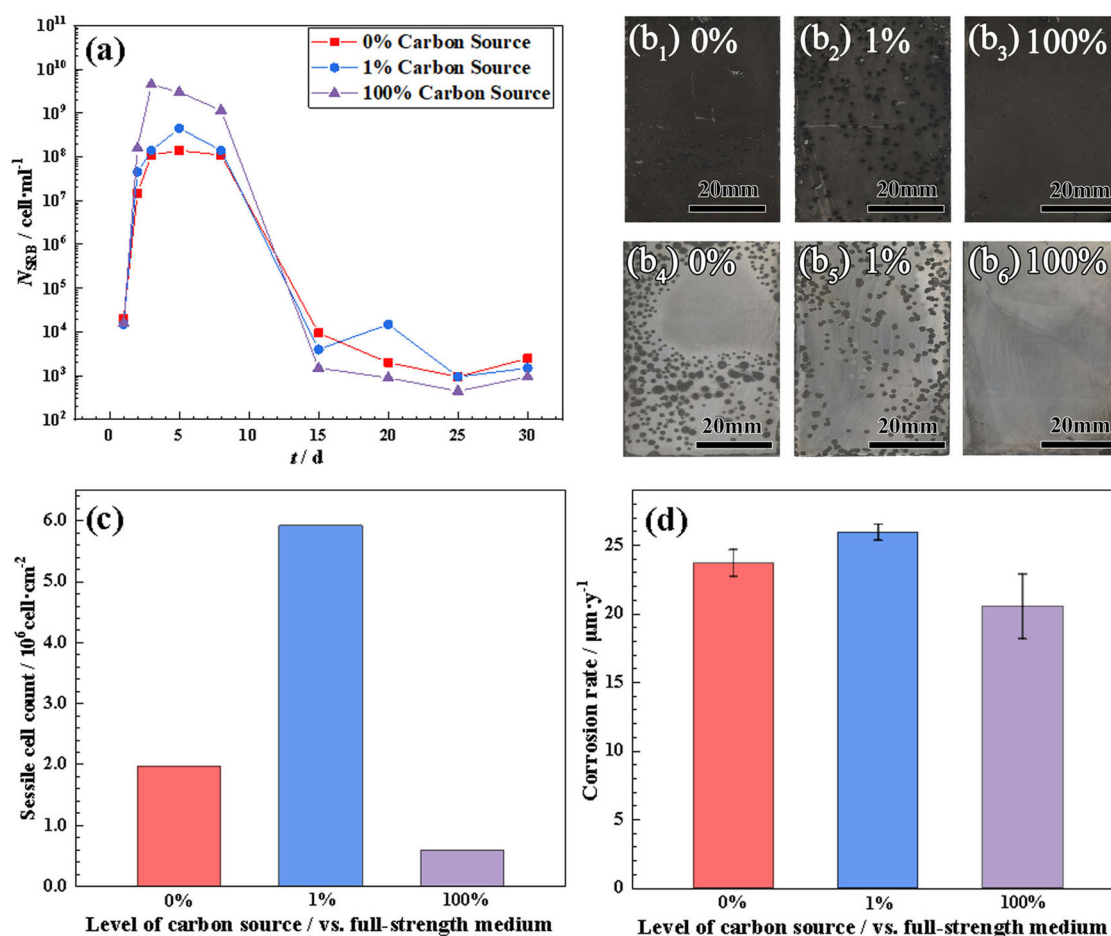


Fig. 2 SRB cell count and corrosion rate of the steel. **a** Shows the number of planktonic SRB cells in the mediums with different levels of organic carbon source. **b1–b6** Show the macroscopic morphologies of the BM surfaces before and after removal of the corrosion product. **c** Shows the number of sessile cells on the BM surfaces in the mediums with different levels of organic carbon source. **d** Shows the corrosion rate of the BM of the welded joint in mediums with different levels of organic carbon source (error bars stand for the standard deviations from three independent sample).

growth curves in limited environments were observed in the three mediums. During the initial phase of the experiment, the number of planktonic SRB cells exponentially increased and reached a peak on 3th day. It remained in the range of 10^8 – 10^{10} cell ml^{-1} on the 3th to 8th days and then began to decline sharply. On the 15th day the SRB number was only about 10^4 cell ml^{-1} and slowly decreased at the end of the experiment. The growth curves of planktonic SRB cells in the mediums with 0 and 1% carbon sources were very similar, but the peak of the SRB number in the mediums with 100% carbon source was 1–2 orders of magnitude larger than those in the mediums with 0 and 1% carbon source. The abundant nutrients in the medium with 100% carbon source supported the propagation of the SRB cells in the stable phase.

The macro-morphologies of the BM surface after 30 d immersion in the three mediums are presented in Fig. 2b₁–b₃. A large number of microbial tubercles were distributed on the BM surfaces in the mediums with 0 and 1% carbon sources, and the number of microbial tubercles in the latter was more than that in the former (Fig. 2b₁, b₂). However, the BM surface was relatively flat in the medium with 100% carbon source (Fig. 2b₃). The facts show that the reduction of carbon source significantly affects the adhesion of SRB cells on the sample surfaces. After removal of the corrosion product, the macro-morphologies of the naked BM surface are presented in Fig. 2b₄–b₆. Dense corrosion spots can be distinctly seen on the BM surface in the mediums of 0 and 1% carbon sources (Fig. 2b₄, b₅), and the positions of the corrosion

spots are in keeping with that of the microbial tubercles as shown in Fig. 2b₁, b₂. However, no obvious corrosion spot was found on the BM surface in the medium with 100% carbon source (Fig. 2b₆).

The numbers of sessile cells on the BM surfaces after 30 d immersion in the three mediums are presented in Fig. 2c. At the end of the experiment, the number of sessile cells on the BM surface was the largest in the medium with 1% carbon source, followed by with 0% carbon source, while that in the medium with 100% carbon source was the smallest one. In the medium with 100% carbon source, SRB exponentially multiplied and thus consumed sharply, resulting into the least SRB cell in the end of the experiment. In the medium with 0% carbon source, SRB cells only relied on sulfate reduction and Fe oxidation to obtain energy, so the survival of the SRB cells was difficult and thus the number of SRB was relatively less. However, in the medium with 1% carbon source, SRB cells can obtain simultaneously electrons from the carbon source and iron matrix. Therefore, more sessile cells existed on the steel surface in this medium. Besides, the numbers of planktonic cells in the three medium was far less than those of sessile cells in the end of the experiment, indicating that bacteria tend to grow on the steel surface at this time. What's more, no reasonable correlation was found between the numbers of planktonic and sessile cells. The fact showed that the number of planktonic cells was not the decisive factor affecting the adhesion of SRB cell on the steel surface.

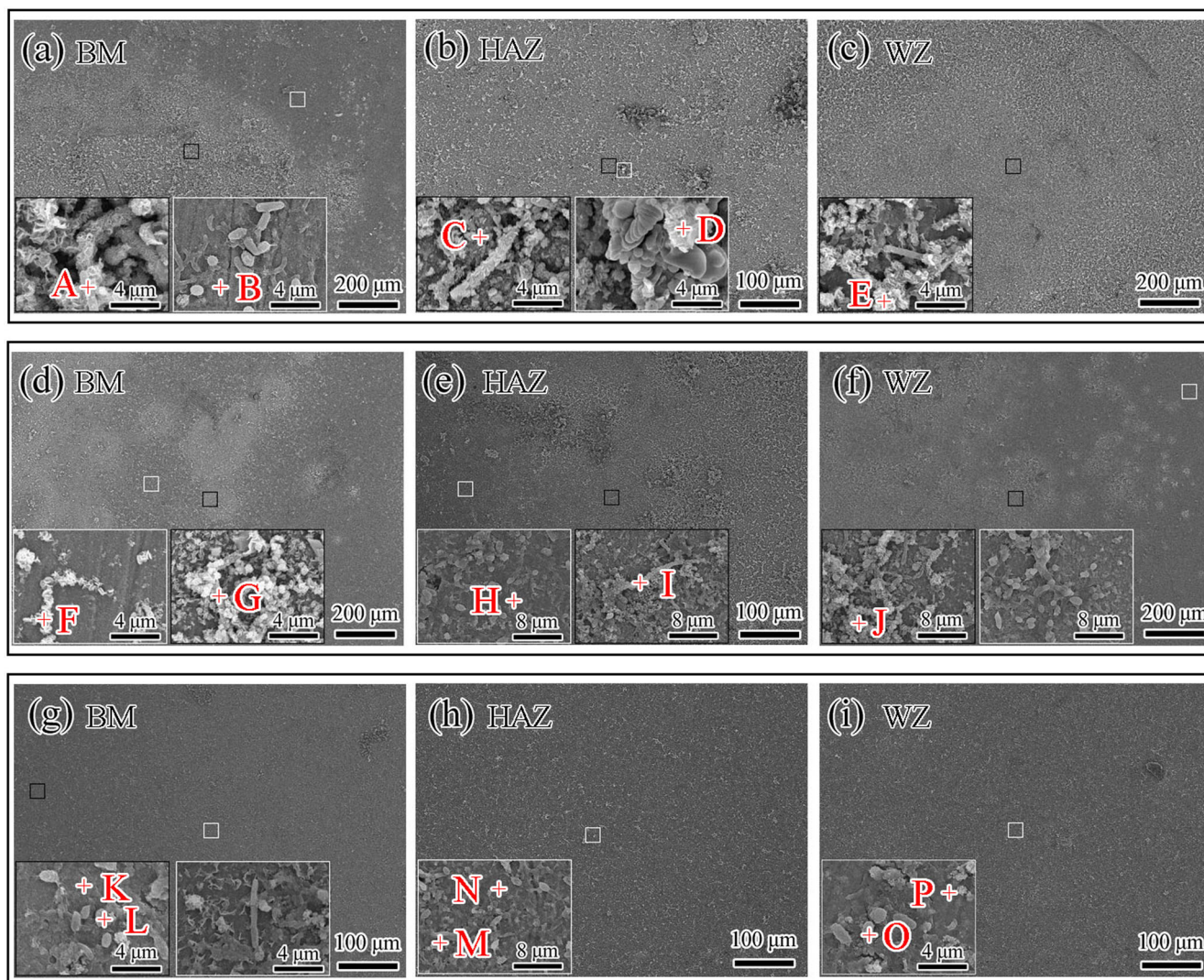


Fig. 3 Micro-morphologies of corrosion products on welded joints after 30 d immersion. **a–c** Show the micro-morphologies of corrosion products on the surfaces of BM, HAZ, and WZ zones in the medium with 0% organic carbon sources level. **d–f** Show the micro-morphologies of corrosion products on the surfaces of BM, HAZ, and WZ zones in the medium with 1% organic carbon sources level. **g–i** Show the micro-morphologies of corrosion products on the surfaces of BM, HAZ, and WZ zones in the medium with 100% organic carbon sources level.

The average corrosion rate of the BM after 30 d immersion in the three mediums are presented in Fig. 2d. The corrosion rate of the BM was the largest in the medium with 1% carbon source, followed by that with 0% carbon source, while that with 100% carbon source was the lowest. The results showed that organic carbon source starvation made SRB more aggressive¹⁶. In the environment with organic carbon source starvation, SRB tended to utilize Fe matrix as an electron donor, promoting the corrosion process of the matrix. In addition, the corrosion rates of the steel were completely identical with the number of sessile SRB cells in the three mediums (Fig. 2c, d), indicating that the number of sessile SRB cells on the steel surface was the decisive factor of the aggressive SRB corrosion for the steel.

Corrosion product on the surface of welded joint

The micro-morphologies of the corrosion products on the surface of BM, HAZ, and WZ after 30 d immersion in the three mediums are shown in Fig. 3, and the corresponding EDS results are listed in Table 1. The surfaces of all samples were covered with a complete mixture of SRB and corrosion products in the three mediums. The distribution of corrosion products on the sample surface in the

mediums with 0 and 1% carbon sources was uneven, and corrosion products and SRB cells varied in different zones. The corrosion products on the sample surface in the medium with 0% carbon source tended to be distributed in flakes, while those with 1% carbon source were mainly distributed in clusters. However, the distribution of corrosion products and SRB on the sample surface in the medium with 100% carbon source was relatively uniform, only with a small amount of prominent corrosion products inlaid on the BM and WZ surfaces. EDS results showed that the relatively higher S content existed in the corrosion products in the medium with 100% level, while the Fe and O contents increased in the corrosion products in the environments with organic carbon source starvation.

The number and morphology of SRB cells on the sample surfaces in the three mediums are of great differences. The number of SRB cells in the product film in the environments with organic carbon source starvation was relatively higher than that in the medium with 100% carbon source, which was consistent with the results of sessile cell counts (Fig. 3c). Besides, the sessile SRB cells in the environments with organic carbon source starvation were mainly slender and stubby, but most of the sessile SRB cells were stubby in the medium with 100% carbon source. The facts

Table 1. EDS results of corrosion products on the surface of BM, HAZ, and WZ for the welded joints (at.%).

Position	O	Fe	S	Si	C
A	54	13	\	5	28
B	30	39	2	\	29
C	43	13	2	10	32
D	40	12	\	6	42
E	52	15	\	7	26
F	49	15	\	5	31
G	48	18	\	\	34
H	45	31	\	\	24
I	38	21	\	\	41
J	33	9	\	4	54
K	9	54	1	\	37
L	25	20	3	\	52
M	31	18	3	2	46
N	16	43	1	\	40
O	33	9	2	1	55
P	12	50	1	\	37

certainly indicated that the general metabolism of starving SRB cells was relatively higher.

The high-resolution spectra of Fe, N, and S orbitals of the corrosion products on the sample surfaces after 30 d immersion in the three medium are presented in Fig. 4. In the medium with 100% carbon source, the corrosion products on the sample surfaces of the welded joint are mainly FeOOH³³, and there is no obvious difference in chemical composition between the three zones (Fig. 4g). However, the species of Fe oxides on the sample surfaces increased in the environments with organic carbon source starvation, containing FeOOH, FeO^{34,35}, Fe₃O₄^{33,36} and Fe₂O₃^{36–38} (Fig. 4a, d). In the same environment, the species of Fe oxides in the BM and WZ were more than those in the HAZ. Besides, many sulfur-containing compounds, such as FeS³⁹, FeS₂^{40,41}, and FePS₃⁴², were detected on the sample surfaces in the three medium, among which FeS and FeS₂ are typical metabolic sulfides of SRB⁴³. In addition, various organic bond pairs^{44,45} also existed in the corrosion products in the sample surface, which may come from the amino acids, constituting proteins, polypeptides, and enzymes in the SRB biofilm²⁸.

Corrosion morphologies of different zones of welded joints

The corrosion morphologies of the surface of BM, HAZ, and WZ after 30 d immersion in the three mediums are shown in Fig. 5. Obviously, the main form of SRB corrosion of the welded joints in the three mediums was localized corrosion, but the degree of corrosion pits were different for different welded zones in different mediums. In the same medium, the diameter and density of corrosion pits in the BM and WZ were always larger than those in the HAZ, indicating that SRB was more inclined to promote localized corrosion in the BM and WZ. SRB corrosion for the welded joint was distinctly selective³². Besides, for the same zone of the welded joint, the diameter and density of corrosion pits on the sample surface were the largest in the medium with 1% carbon source, followed by that with 0% carbon source, with it was the smallest in the medium with 100% carbon source. Especially, in the medium with 100% carbon source, there was almost no corrosion pit existing in the HAZ (Fig. 5h). The aggressiveness of the SRB cells to the welded joint was strongest in the medium with 1% carbon source, significantly promoting the localized corrosion of the welded joints. Therefore, SRB corrosion

of the welded joint was selective, and organic carbon source starvation increased its selective characteristics.

3D morphologies of the surfaces of BM, HAZ, and WZ after 30 d immersion in the three mediums are presented in Fig. 6. Obviously, the localized corrosion susceptibility of the HAZ was always less than those of the BM and WZ in the same medium. For the same zone in the welded joint, the corrosion degree of the sample in the medium with 1% carbon source was more severe. The facts were in complete agreement with the corrosion morphologies of the samples. The depths of 5 random corrosion pits on the surface of each sample were recorded, and the average depth of their corrosion pits of the samples are shown in Fig. 7. For the same zone in the welded joint, the average depths of the corrosion pits in the mediums with 0 and 1% carbon sources were about 1.5 and 2.5 times of that with 100% carbon source, respectively. Organic carbon source starvation-induced SRB to accelerate the corrosion of the welded joint, and the acceleration effect was more obvious in the medium with 1% carbon source. In all mediums, the average depth of the corrosion pits in the WZ was about 3.5–4.0 times of that in the HAZ, while it became 4.5–6.5 times in the BM. The selectivity of the SRB corrosion for the welded joints varied in different medium.

DISCUSSION

From Fig. 2b, d, organic carbon source starvation-induced SRB corrosion and promoted the localized corrosion susceptibility of the welded joint. In order to quantitatively describe the effect of organic carbon source starvation on SRB corrosion acceleration of welded joints, the uniform corrosion acceleration factor (k_{CR}) and pitting corrosion acceleration factor (k_{pit}) were defined using the average corrosion rate and the average depth of the corrosion pits. k_{CR} and k_{pit} can be expressed as follows:

$$k_{CR} = \frac{CR}{CR_0} \quad (4)$$

$$k_{pit} = \frac{l}{l_0} \quad (5)$$

where, CR and CR₀ are the average corrosion rates of the BM in the mediums with organic carbon source starvation and in the medium with 100% carbon source, respectively. l and l_0 represent the average depth of the corrosion pits of the samples in the mediums with organic carbon source starvation and in the medium with 100% carbon source, respectively. Obviously, both k_{CR} and k_{pit} were equal to 1 in the medium with 100% carbon source. This method has been widely used in the studies of corrosion and pitting behavior of metallic materials^{46–50}.

Figure 8 presents the acceleration factors of SRB corrosion in the BM of welded joints in the three mediums. In the mediums with 0 and 1% carbon sources, k_{CR} of the BM were 1.15 and 1.26, while k_{pit} of the BM were 1.75 and 3.33, respectively. This result shows that the starving SRB cells accelerated simultaneously the uniform corrosion and localized corrosion of the welded joints, and the accelerated SRB corrosion was more obvious in the medium with 1% carbon source. Besides, k_{pit} of the BM was much larger than its corresponding k_{CR} under the same carbon source starvation. The accelerated SRB corrosion was more embodied in k_{pit} rather than k_{CR} . Therefore, k_{pit} was selected to analyze the effect of organic carbon source starvation on SRB accelerated corrosion of the welded joint hereinafter.

Given that the above results were merely relative to the BM of the welded joint, did the organic carbon source starvation have the same influence on SRB corrosion of the HAZ and WZ? To answer this question, k_{pit} of the HAZ and WZ in the three mediums were calculated according to the Eq. (5), and the results are presented in Fig. 9. Under organic carbon source starvation, k_{pit} of all zones were greater than 1, showing that the organic carbon

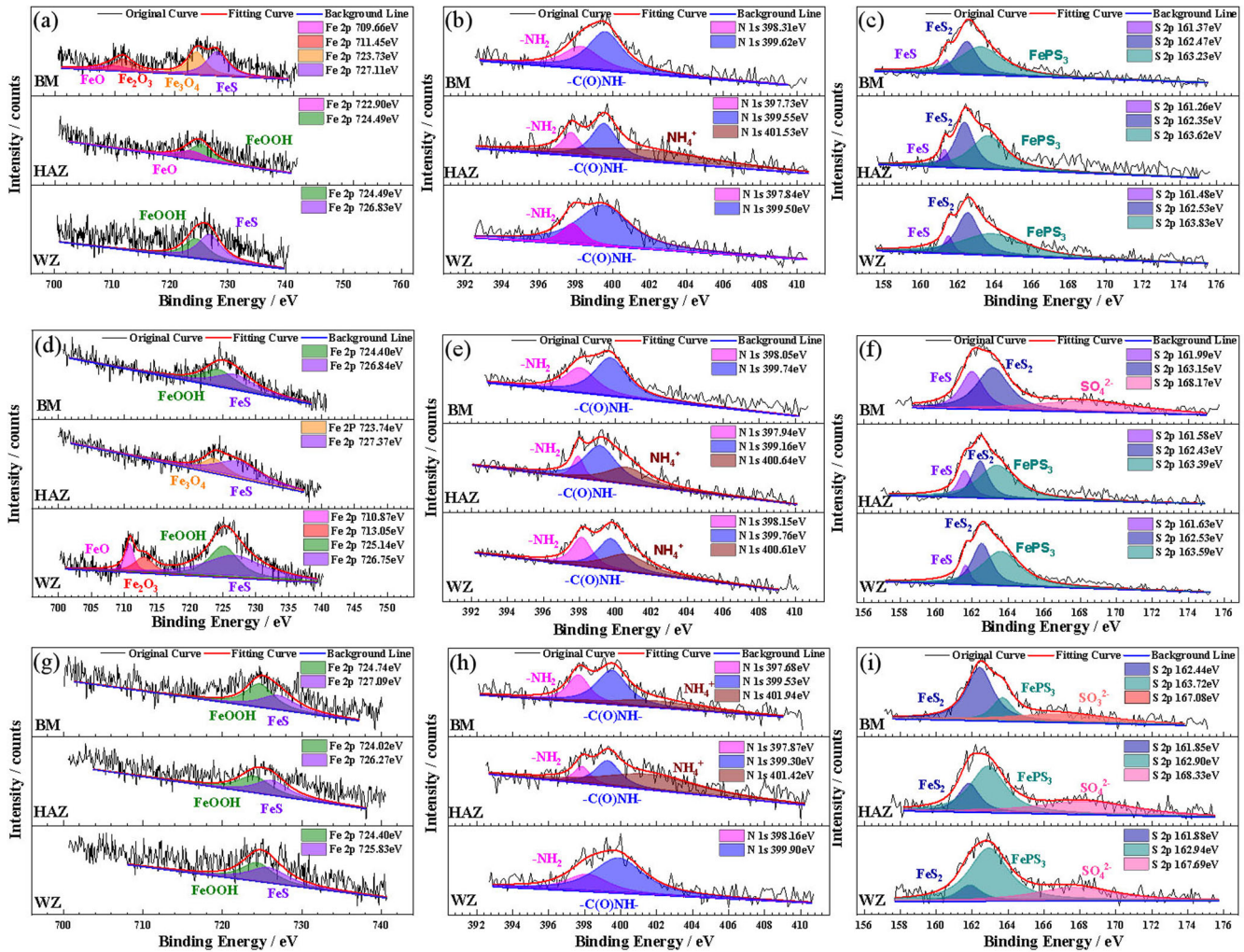


Fig. 4 XPS spectra of corrosion products on welded joints after 30 d immersion. **a–c** Show the XPS spectra of corrosion products on the welded joints in the medium with 0% organic carbon sources level. **d–f** Show the XPS spectra of corrosion products on the welded joints in the medium with 1% organic carbon sources level. **g–i** Show the XPS spectra of corrosion products on the welded joints in the medium with 100% organic carbon sources level.

source starvation accelerated the localized pits in the SRB corrosion of the welded joint. In the environments with organic carbon source starvation, the starving SRB used carbon steel as an electron donor and preferentially attached to the sample. Then, many microbial tubercles will be generated on the sample surface (Fig. 2b), resulting in the increased corrosion rate of the steel (Fig. 2d) and the severe corrosion pits on the sample surfaces (Fig. 5). Besides, κ_{pit} of the samples in the medium with 1% carbon source were greater than that with 0% carbon source, revealing the more obvious acceleration effect in the medium with 1% carbon source. In the medium with 0% carbon source, the number of planktonic and sessile SRB cells was less. Thus, the aggressiveness of SRB cells to the iron matrix was relatively weak. However, in the medium with 1% carbon source, SRB can obtain electrons from both carbon source and iron matrix. Thus, the metabolism of SRB was relatively vigorous (Fig. 3), and the number of sessile SRB cells was relatively large (Fig. 2). Under the mature biofilm, the starving SRB cells were more aggressive to the iron matrix and promoted more serious localized corrosion on the sample surfaces.

As shown in Figs. 5 and 9, SRB corrosion and κ_{pit} of different zones varied with organic carbon source starvation. In other words, the influence of organic carbon source starvation on the selectivity of SRB corrosion was different for different zones of the welded joint. To quantitatively describe the influence, a selectivity

factor (K_{select}) was defined using the average pit depth. Given that the localized corrosion susceptibility of the HAZ was always the lowest in all mediums, the average pit depth of the HAZ was used as a reference standard and thus K_{select} can be expressed as follows:

$$K_{\text{select}} = \frac{l}{l_{\text{HAZ}}} \quad (6)$$

where, l is the average pit depth in the BM or WZ and l_{HAZ} is the average pit depth of the HAZ in the same medium, respectively. Obviously, K_{select} of the HAZ was equal to 1 in all mediums.

The calculated K_{select} of SRB corrosion for the welded joints in the three mediums are shown in Fig. 10. K_{select} for the BM and WZ in the medium with 100% carbon source were far greater than 1, indicating that SRB corrosion of welded joints was intensively selective. K_{select} for the HAZ and BM were respectively the smallest and the largest in this medium, which is consistent with our previous results³². K_{select} for the BM and WZ in the mediums with 0 and 1% carbon sources were respectively greater than those in the medium with 100% carbon source, and K_{select} for the BM and WZ were the largest in the medium with 1% carbon source. The facts showed that organic carbon source starvation improved the selectivity of SRB corrosion of welded joints, and the selectivity was most significant in the medium with 1% carbon source.

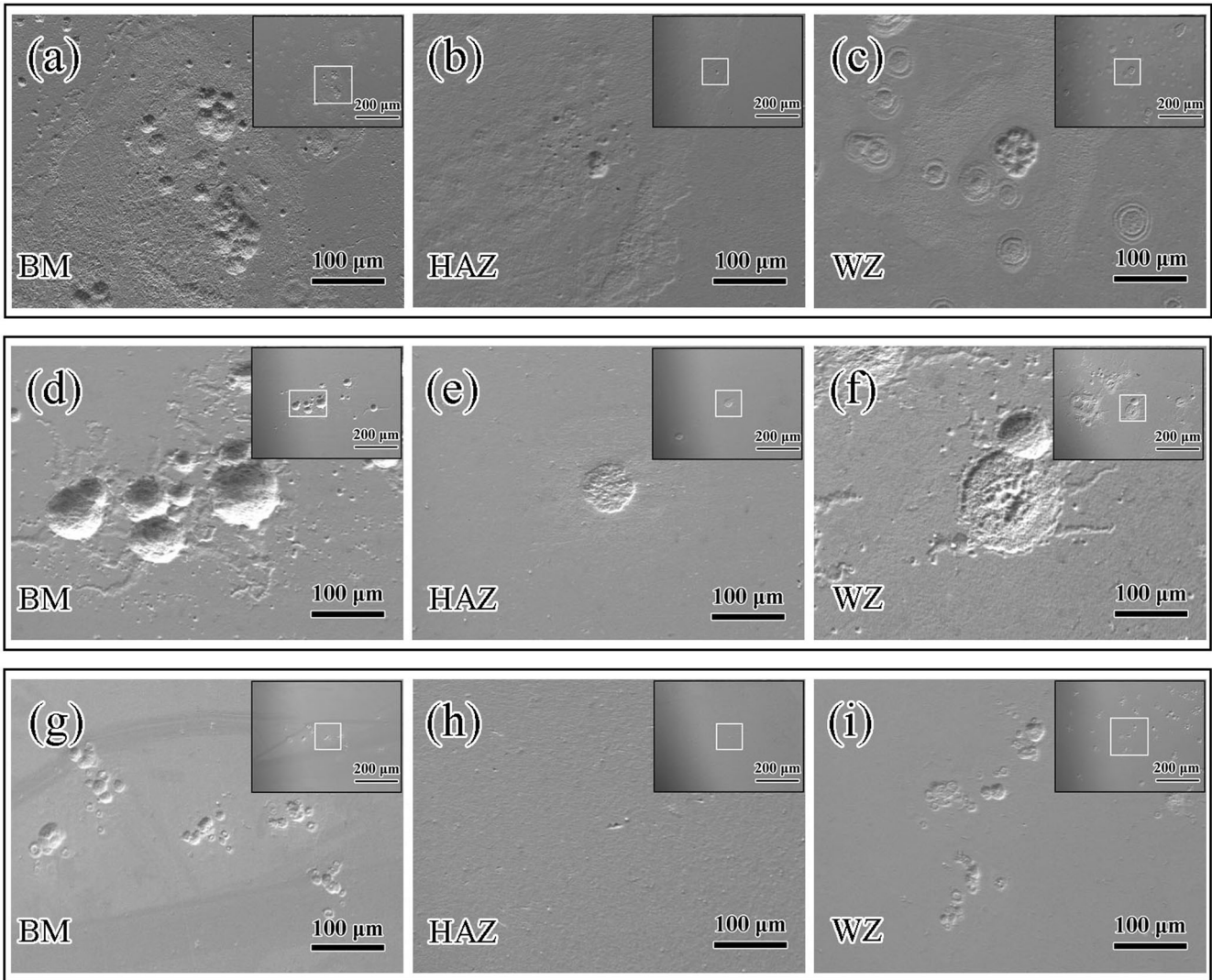


Fig. 5 Corrosion morphology of welded joints after 30 d immersion. **a–c** Show the corrosion morphology of BM, HAZ, and WZ zones after 30 d immersion in the medium with 0% organic carbon sources level. **d–f** Show the corrosion morphology of BM, HAZ, and WZ zones after 30 d immersion in the medium with 1% organic carbon sources level. **g–i** Show the corrosion morphology of BM, HAZ and WZ zones after 30 d immersion in the medium with 100% organic carbon sources level.

However, in all mediums, K_{select} for the HAZ was always smallest, following by that for the WZ, while that for BM was largest. Organic carbon source starvation improved the selectivity of SRB corrosion of welded joints, but did not change the order of this selectivity.

As shown in Fig. 11, the main micro-structures of the BM are uniformly distributed polygonal ferrite and bainite (Fig. 11a, d, and g), while that in the HAZ is the granular bainite structures with coarse grains and obvious grain boundaries dominate the (Fig. 11b, e, and h). The WZ is composed of fine ferrite with coarse feathered Widmanstatten structures (Fig. 11c, f, and i). It was reported that the grain boundaries in metal have the characteristics of high density dislocation, high intrinsic energy, and low electron work function^{51,52}. Thus, it is easy for bacteria to obtain electrons and hence adhere near or to the grain boundaries^{30,53}. Therefore, SRB prefers to use the BM or WZ of the welded joint as the electron donor. In the mediums with carbon source starvation, SRB turns to iron matrix to obtain electrons. It is a reasonable speculation that the starving SRB more liked to obtain electrons from the zones with high intrinsic energy and low electron work function, leading to more serious SRB corrosion in the BM and WZ of the welded joint in the mediums with organic carbon source

starvation. On the other hand, the number and active metabolism of SRB cells may be relatively higher in the BM and WZ with high intrinsic energy and low electron work function (Figs. 2c and 3) under the level of organic carbon source starvation. Thus, SRB were more aggressive against iron matrix. Under the combined action of the above two factors, organic carbon source starvation promoted the selectivity of SRB corrosion of welded joints.

METHODS

Materials

A spirally welded joint of X80 pipeline steel was selected as the experimental sample in this work, with the composition of the pipeline steel (wt.%): C 0.0466, Si 0.204, Mn 7.154, P 0.0082, S 0.0009, Ni 0.206, Cr 0.235, Cu 0.174, Nb 0.524, V 0.0022, Ti 0.0142, Mo 0.125, Al 0.0265, B 0.0004, and Fe Bal. Three zones (BM, HAZ, and WZ) of the welded joint were processed by wire cutting. Three groups of the BM, HAZ, and WZ samples were taken for carbon starvation experiments with different carbon sources. Due to the small zones of the WZ and HAZ in the welded joint, the weight loss measurement and sessile counts were only performed on the

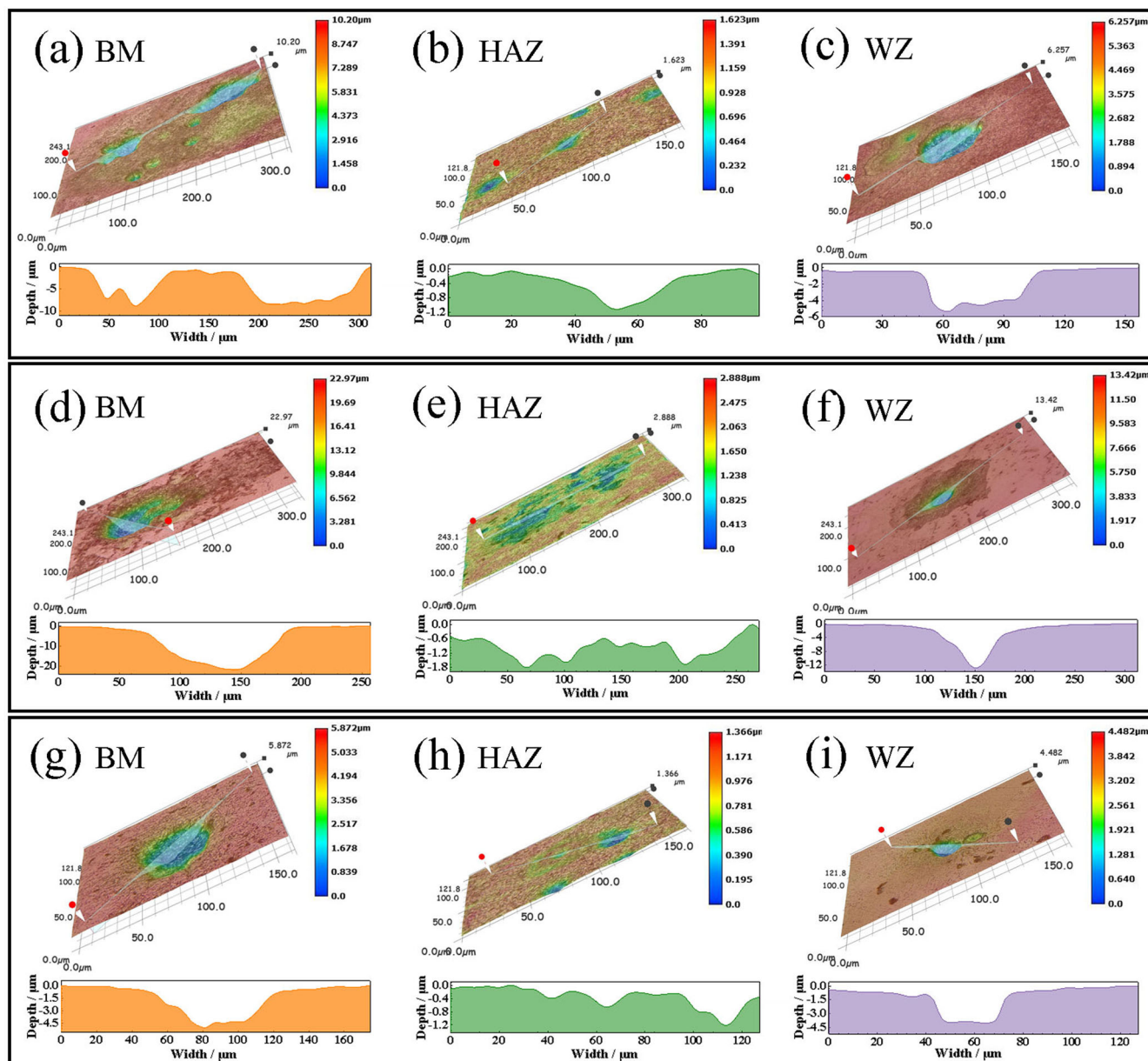


Fig. 6 3D ultra-depth micro-morphology of the welded joints after 30 d immersion. **a–c** Show the 3D ultra-depth micro-morphology of BM, HAZ, and WZ zones after 30 d immersion in the medium with 0% organic carbon sources level. **d–f** Show the 3D ultra-depth micro-morphology of BM, HAZ, and WZ zones after 30 d immersion in the medium with 1% organic carbon sources level. **g–i** Show the 3D ultra-depth micro-morphology of BM, HAZ and WZ zones after 30 d immersion in the medium with 100% organic carbon sources level.

BM samples. The working surfaces of all samples were gradually polished from 280# to 1200# with water-resistant sandpaper, rinsed repeatedly with deionized water and anhydrous ethanol, and then blown dry in cold air for use. Before the experiment, all samples were sterilized by ultraviolet light in a vacuum glove box.

The SRB strains selected in this study were consistent with the previous experiments⁵⁴. The SRB strains were cultivated in the ATCC 1249 medium and the 3rd generation strain was used for the follow-up experiment. The composition of the ATCC 1249 medium was shown in Table 2. In this study, modified ATCC 1249 medium was used as the experiment solution, and the contents of carbon sources including trisodium citrate and sodium lactate were controlled at 0%, 1%, and 100%, respectively. The three mediums with different levels of carbon source were sterilized in an autoclave at 121 °C for 30 min, and then deoxygenated by high-purity nitrogen for 2 h. In these mediums, yeast extract

contains a small amount of organic carbon, which can provide growth factors and vitamins for SRB metabolism in the medium with 0% carbon source.

Experimental procedure

The samples pre-polished via water-resistant sandpaper were divided into three groups and pre-immersed in anaerobic flasks with 1 L full carbon source medium containing SRB. After 3 d pre-incubation, the samples with mature biofilms were taken out from the flasks and the planktonic cells on the sample surfaces were washed away with sterile and deoxygenated phosphate-buffered saline (PBS) solution. Then the three groups of samples were respectively immersed into anaerobic flasks with 1 L medium with 0%, 1%, and 100% carbon source. After that, the flasks were immediately sealed using silica gel. During the experiment, planktonic cell counts in the three mediums were measured at

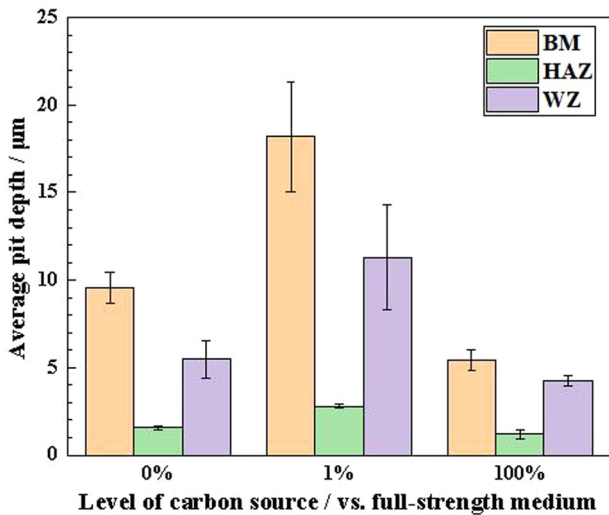


Fig. 7 Average pit depth of welded joints after 30 d immersion. The figure shows the average pit depth of BM, HAZ, and WZ for the welded joints after the 30d immersion in different organic carbon source medium (error bars stand for the standard deviations from three independent sample).

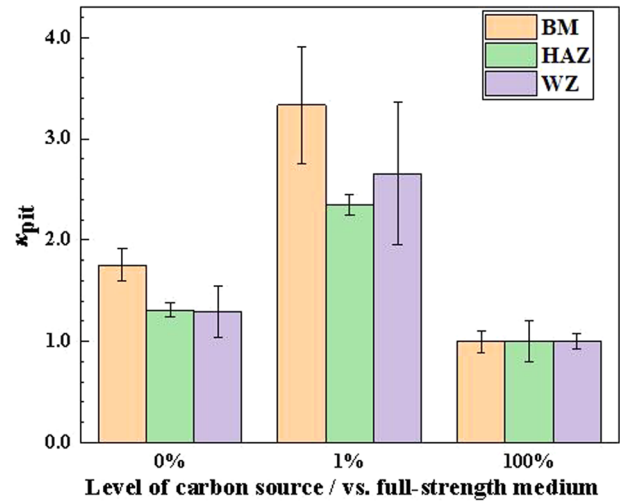


Fig. 9 K_{pit} for welded joints. The figure shows K_{pit} of organic carbon source starvation on SRB corrosion of BM, HAZ, and WZ for the welded joints (error bars stand for the standard deviations from three independent sample).

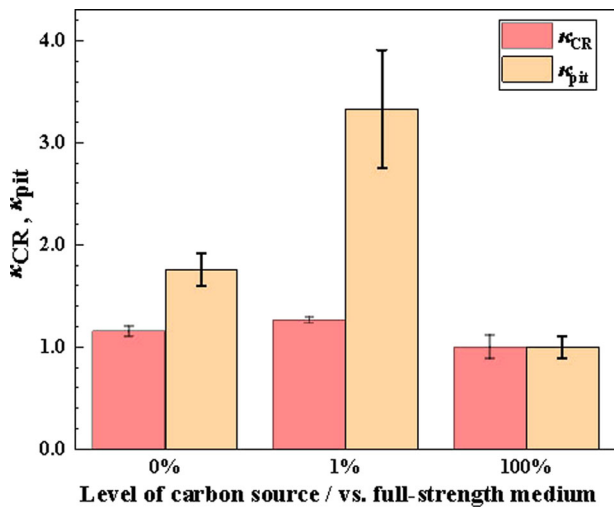


Fig. 8 K_{CR} and K_{pit} for BM zone. The figure shows K_{CR} and K_{pit} of organic carbon source starvation on corrosion of BM for the welded joints (error bars stand for the standard deviations from three independent sample).

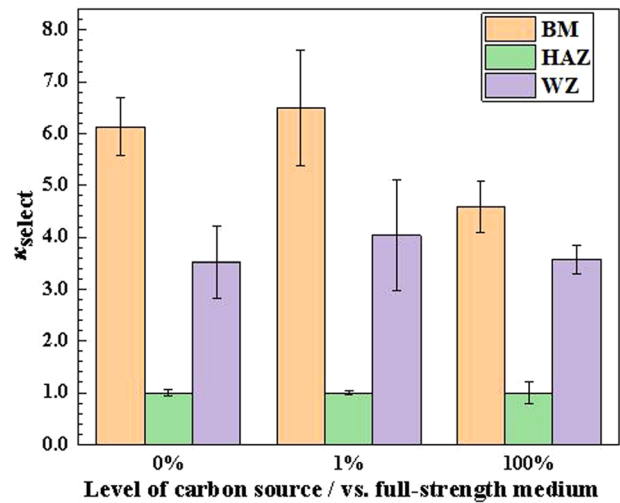


Fig. 10 K_{select} of SRB corrosion for welded joints. The figure shows K_{select} of SRB corrosion of the welded joints in the mediums with different organic carbon source starvation (error bars stand for the standard deviations from three independent sample).

intervals. After 30 d immersion, three groups of samples were taken out from the flasks, immersed with 5.0 wt.% glutaraldehyde for 5 h to fix the biofilm. Then, they were dehydrated successively by 30, 50, 70, and 100 vol.% anhydrous ethanol, dried, and placed in a sterile glove box for subsequent experiments. Beside, after 30 d immersion, another three BM samples that were just taken out from the flasks were used for sessile cells count and weight loss experiments, respectively. All the experimental procedures were conducted in a glove box full of high-purity nitrogen.

Bacteria count

In this work, KBC bacteria test flasks were used to measure planktonic cells in medium and sessile cells on the sample surface. The flasks was designed for the most probable number (MPN) method according to GB/T 14643.5-2009. During the experiment, 3 ml of solution was extracted from the anaerobic flasks at intervals to determine the planktonic SRB cell count and the

results were reported using the unit of is cell ml^{-1} . After the experiment, three BM samples were taken out from the flasks, and shook in a conical flask with 100 mL of deoxygenated PBS solution for 2 h. Then, 3 ml of the PBS solution was used to determine the sessile SRB cell count and the results were reported using the unit of is cell cm^{-2} .

Weight loss analysis

Before the experiment, an analytical balance with an accuracy of 0.0001 g was used to recorded the initial weight of the BM samples. After the 30 d immersion, the corrosion products on the sample surfaces were removed using a rust remover consisting of 500 mL hydrochloric acid (18 wt.%), 500 mL deionized water, and 3.5 g hexamethylenetetramine. The final weight of the samples were determined again with the same analytical balance, and the

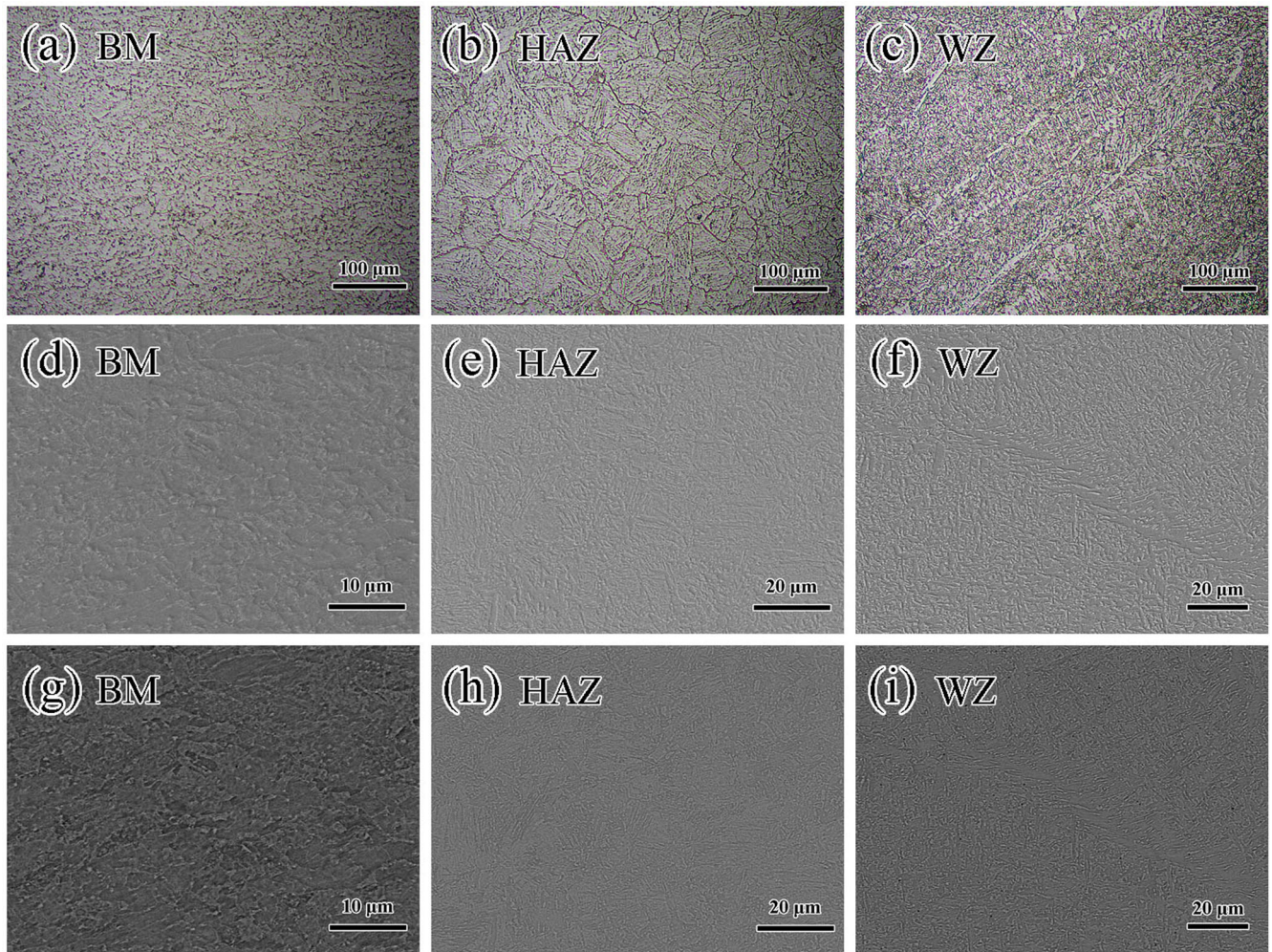


Fig. 11 Microstructures of welded joints. **a–c** Show the metallographic photos of the welded joints. **d–f** Show the secondary electron images of the welded joints. **g–i** Show the backscattered electron images of the welded joints.

Table 2. Chemical composition of 1L ATCC1249 medium.		
Component I	MgSO ₄	2.0 g
	Na ₃ C ₆ H ₅ O ₇	5.0 g
	CaSO ₄	1.0 g
	NH ₄ Cl	1.0 g
	Distilled water	400 ml
Component II	K ₂ HPO ₄	0.5 g
	Distilled water	200 ml
Component III	NaC ₃ H ₅ O ₃	3.5 g
	Yeast extract	1.0 g
	Distilled water	400 ml
Component IV	Filter-sterilized 5 wt. % (NH ₄) ₂ Fe(SO ₄) ₂ Add 0.1 ml of this solution to 5.0 ml of medium prior to inoculation	

corrosion rate was calculated as follows¹⁵:

$$v_{\text{corr}} = \frac{K \times \Delta m}{\rho \times S \times t} \quad (7)$$

Where v_{corr} is the corrosion rate (mm^{-1}), K is the unit constant (87,600), Δm is the average weight loss of three replicate samples (g), and ρ is the density of the sample (7.85 g cm^{-3}), S is the working

area of the sample (cm^2), t represents the immersing time (h), respectively.

Micro-morphology and composition characterization

After the 30 d immersion, the samples were treated according to the procedure in section 2.3. X-ray photoelectron spectroscopy (XPS, ESCALAB250XI surface analysis system, Thermo VG, USA) was used to determine the chemical state of the elements in the corrosion products. The binding energy in the high-resolution spectra was corrected referring to the C_{1s} sub-peak at 284.6 eV and the sub-peaks in the XPS spectra were separated using XPSPEAK4.1 software. Then the sample surfaces were sprayed with gold for 120 s to increase the electrical conductivity of the corrosion products, and then the morphology of the corrosion products on the sample surfaces was observed by scanning electron microscope (SEM, Zeiss EVO). The ingredients of the corrosion products on the sample surface were analyzed by energy dispersive spectroscopy (EDS, OXFORD X-Max^N) as well. After that, the corrosion products were removed using the same rust remover from the sample surfaces, and the corrosion morphology of the samples was detected by SEM. Finally, the 3D morphology of the corroded surfaces and the corrosion pit on it were reconstructed using 3D ultra-depth microscopy (VHX-2000).

DATA AVAILABILITY

The data presented in this article is available upon request to the authors.

CODE AVAILABILITY

No code was used in this work.

Received: 18 April 2022; Accepted: 27 August 2022;

Published online: 27 September 2022

REFERENCES

- Zhang, P., Xu, D., Li, Y., Yang, K. & Gu, T. Electron mediators accelerate the microbiologically influenced corrosion of 304 stainless steel by the *Desulfovibrio vulgaris* biofilm. *Bioelectrochemistry* **101**, 14–21 (2015).
- Liu, H., Gu, T., Zhang, G., Liu, H. & Cheng, Y. F. Corrosion of X80 pipeline steel under sulfate-reducing bacterium biofilms in simulated CO₂-saturated oilfield produced water with carbon source starvation. *Corros. Sci.* **136**, 47–59 (2018).
- Wu, T. et al. Stress corrosion of pipeline steel under disbonded coating in a SRB-containing environment. *Corros. Sci.* **157**, 518–530 (2019).
- Ma, Y. et al. Microbiologically influenced corrosion of marine steels within the interaction between steel and biofilms: A brief view. *Appl. Microbiol. Biotechnol.* **104**, 515–525 (2020).
- Zhou, E. et al. A novel Cu-bearing high-entropy alloy with significant antibacterial behavior against corrosive marine biofilms. *J. Mater. Sci. Technol.* **46**, 201–210 (2020).
- Xu, D. et al. Accelerated corrosion of 2205 duplex stainless steel caused by marine aerobic *Pseudomonas aeruginosa* biofilm. *Bioelectrochemistry* **113**, 1–8 (2017).
- Javaherdashti, R. *Microbiologically Influenced Corrosion: An Engineering Insight*. Springer: Cham. 123–131 (2008).
- AlAbbas, F. M. et al. Influence of sulfate reducing bacterial biofilm on corrosion behavior of low-alloy, high-strength steel (API-5L X80). *Int. Biodeterior. Biodegrad.* **78**, 34–42 (2013).
- Tang, H. Y. et al. Stainless steel corrosion via direct iron-to-microbe electron transfer by *Geobacter* species. *ISME J.* **15**, 3084–3093 (2021).
- Zhou, X. et al. Accelerated tidal corrosion of X80 pipeline steel by *Desulfovibrio desulfuricans*. *Corros. Sci.* **201**, 110272 (2022).
- Wu, T. et al. Microbiologically induced corrosion of X80 pipeline steel in an acid soil solution: (I) Electrochemical analysis. *J. Chin. Soc. Corros. Prot.* **34**, 346–352 (2014).
- Wu, T. et al. Microbiologically induced corrosion of X80 pipeline steel in an acid soil solution: (II) Corrosion morphology and corrosion product analysis. *J. Chin. Soc. Corros. Prot.* **34**, 353–358 (2014).
- Chen, Y. et al. Long-term survival of *Desulfovibrio vulgaris* on carbon steel and associated pitting corrosion. *Corros. Sci.* **90**, 89–100 (2015).
- Zhou, X., Zhou, Z., Wu, T., Li, C. & Li, Z. Effects of non-viable microbial film on corrosion of pipeline steel in soil environment. *Corros. Commun.* **3**, 23–33 (2021).
- Fan, Y. et al. Early corrosion behavior of X80 pipeline steel in a simulated soil solution containing *Desulfovibrio desulfuricans*. *Bioelectrochemistry* **141**, 107880 (2021).
- Xu, D. & Gu, T. Carbon source starvation triggered more aggressive corrosion against carbon steel by the *Desulfovibrio vulgaris* biofilm. *Int. Biodeterior. Biodegrad.* **91**, 74–81 (2014).
- Li, Y. et al. Anaerobic microbiologically influenced corrosion mechanisms interpreted using bioenergetics and bioelectrochemistry: A review. *J. Mater. Sci. Technol.* **34**, 1713–1718 (2018).
- Chastain, B. K. & Kral, T. A. Zero-valent iron on Mars: An alternative energy source for methanogens. *Icarus* **208**, 198–201 (2010).
- Ginner, J. L., Alvarez, P. J. J., Smith, S. L. & Scherer, M. M. Nitrate and nitrite reduction by Fe⁰: Influence of mass transport, temperature, and denitrifying microbes. *Environ. Eng. Sci.* **21**, 219–229 (2004).
- Liu, H. & Frank Cheng, Y. Mechanism of microbiologically influenced corrosion of X52 pipeline steel in a wet soil containing sulfate-reduced bacteria. *Electrochim. Acta* **253**, 368–378 (2017).
- Jia, R. et al. Effects of biogenic H₂S on the microbiologically influenced corrosion of C1018 carbon steel by sulfate reducing *Desulfovibrio vulgaris* biofilm. *Corros. Sci.* **130**, 1–11 (2018).
- Jia, R. et al. Effects of ferrous ion concentration on microbiologically influenced corrosion of carbon steel by sulfate reducing bacterium *Desulfovibrio vulgaris*. *Corros. Sci.* **153**, 127–137 (2019).
- Xu, D., Li, Y., Song, F. & Gu, T. Laboratory investigation of microbiologically influenced corrosion of C1018 carbon steel by nitrate reducing bacterium *Bacillus licheniformis*. *Corros. Sci.* **77**, 385–390 (2013).
- Nan, L., Xu, D., Gu, T., Song, X. & Yang, K. Microbiological influenced corrosion resistance characteristics of a 304L-Cu stainless steel against *Escherichia coli*. *Mater. Sci. Eng., C* **48**, 228–234 (2015).
- Jiang, J. et al. Effects of aging time on intergranular and pitting corrosion behavior of Cu-bearing 304L stainless steel in comparison with 304L stainless steel. *Corros. Sci.* **113**, 46–56 (2016).
- Guan, F. et al. Synergistic effect of carbon starvation and exogenous redox mediators on corrosion of X70 pipeline steel induced by *Desulfovibrio singaporensis*. *Sci. Total Environ.* **788**, 147573 (2021).
- Xu, D., Li, Y. & Gu, T. Mechanistic modeling of biocorrosion caused by biofilms of sulfate reducing bacteria and acid producing bacteria. *Bioelectrochemistry* **110**, 52–58 (2016).
- Li, Y. et al. Bacterial distribution in SRB biofilm affects MIC pitting of carbon steel studied using FIB-SEM. *Corros. Sci.* **167**, 108512 (2020).
- Dou, W. et al. Electrochemical investigation of increased carbon steel corrosion via extracellular electron transfer by a sulfate reducing bacterium under carbon source starvation. *Corros. Sci.* **150**, 258–267 (2019).
- Nandakumar, K., Sreekumari, K. R. & Kikuchi, Y. Grain boundary effect on bacterial attachment (Materials, Metallurgy & Weldability). *Trans. Jwri.* **30**, 79–88 (2001).
- Zhu, L. Microbiological influenced corrosion of X80 pipeline and weld microstructure. Shenyang: *Shenyang University of Technology*. 14–35 (2020).
- Wang, Q. et al. Selected corrosion of X80 pipeline steel welded joints induced by *D. desulfuricans*. *Corros. Sci.* **202**, 110313 (2022).
- Tan, B. J., Klabunde, K. J. & Sherwood, P. A. X-ray photoelectron spectroscopy studies of solvated metal atom dispersed catalysts. Monometallic iron and bimetallic iron-cobalt particles on alumina. *J. Am. Chem. Soc.* **113**, 855–861 (1991).
- Mills, P. & Sullivan, J. L. A study of the core level electrons in iron and its three oxides by means of X-ray photoelectron spectroscopy. *J. Phys. D: Appl. Phys.* **16**, 723 (1983).
- McIntyre, N. S. & Zetaruk, D. G. X-ray photoelectron spectroscopic studies of iron oxides. *Anal. Chem.* **49**, 1521–1529 (1977).
- Allen, G. C., Curtis, M. T. & Hooper, A. J. X-ray photoelectron spectroscopy of iron-oxygen systems. *J. Chem. Soc., Dalton Trans.* **14**, 1525–1530 (1974).
- Langevoort, J. C., Sutherland, I. & Hanekamp, L. J. On the oxide formation on stainless steels AISI 304 and incoloy 800H investigated with XPS. *Appl. Surf. Sci.* **28**(2), 167–179 (1987).
- Carver, J. C., Schweitzer, G. K. & Carlson, T. A. Use of X-ray photoelectron spectroscopy to study bonding in Cr, Mn, Fe, and Co compounds. *J. Chem. Phys.* **57**, 973–982 (1972).
- Binder, H. ESCA-Untersuchungen an Eisen-Schwefelverbindungen. *Z. Naturforsch., B: Chem. Sci.* **28**, 255–262 (1973).
- Heide, H. V. D., Hemmel, R. & Bruggen, C. F. V. X-ray photoelectron spectra of 3d transition metal pyrites. *J. Solid State Chem.* **33**, 17–25 (1980).
- Laajalehto, K., Kartio, I. & Nowak, P. XPS study of clean metal sulfide surfaces. *Appl. Surf. Sci.* **81**, 11–15 (1994).
- Ichimura, K. & Sano, M. Electrical conductivity of layered transition-metal phosphorus trisulfide crystals. *Synth. Met.* **45**, 203–211 (1991).
- Wei, B. et al. Effect of sulfate-reducing bacteria on corrosion of X80 pipeline steel under disbonded coating in a red soil solution. *J. Mater. Sci. Technol.* **87**, 1–17 (2021).
- Nefedov, V. I., Salyin, Y. V. & Solozhenkin, P. M. X-ray photoelectron study of surface compounds formed during flotation of minerals. *Surf. Interface Anal.* **2**, 170–172 (1980).
- Uchida, E., Uyama, Y. & Iwata, H. XPS analysis of the poly (ethylene terephthalate) film grafted with acrylamide. *J. Polym. Sci., Part A: Polym. Chem.* **28**, 2837–2844 (1990).
- Wang, Y., Xu, L., Sun, J. & Frank Cheng, Y. Mechano-electrochemical interaction for pipeline corrosion: A review. *J. Pipeline Sci. Eng.* **1**, 1–16 (2021).
- Wang, D. et al. Distinguishing two different microbiologically influenced corrosion (MIC) mechanisms using an electron mediator and hydrogen evolution detection. *Corros. Sci.* **177**, 108993 (2020).
- Sun, J. Development of finite element-based models for defect assessment on pipelines. Calgary: *University of Calgary* (2020).
- Xu, J., Jia, R., Yang, D., Sun, C. & Gu, T. Effects of D-Phenylalanine as a biocide enhancer of THPS against the microbiologically influenced corrosion of C1018 carbon steel. *J. Mater. Sci. Technol.* **35**, 109–117 (2019).
- Gu, T., Jia, R., Unsal, T. & Xu, D. Toward a better understanding of microbiologically influenced corrosion caused by sulfate reducing bacteria. *J. Mater. Sci. Technol.* **35**, 631–636 (2019).
- Li, R. et al. Microstructure and properties of reactive plasma sprayed nano-Ti_xCr_{1-x}N ceramic coating. *Surf. Coat. Technol.* **391**, 125658 (2020).

52. Lu, H., Li, L., Huang, X. & Li, D. An electron work function based mechanism for solid solution hardening. *J. Alloy Compd.* **737**, 323–329 (2018).
53. Javed, M. A., Stoddart, P. R., McArthur, S. L. & Wade, S. A. The effect of metal microstructure on the initial attachment of *Escherichia coli* to 1010 carbon steel. *Biofouling* **29**, 939–952 (2013).
54. Wu, T. et al. Hydrogen permeation of X80 steel with superficial stress in the presence of sulfate-reducing bacteria. *Corros. Sci.* **91**, 86–94 (2015).

ACKNOWLEDGEMENTS

We are grateful for financial support of National Natural Science Foundation of China (51971191, 51601164), Provincial Key R&D Program of Hunan (2021GK2008), and Hunan Provincial Natural Science Foundation of China (2019JJ30023, 2019RS2038).

AUTHOR CONTRIBUTIONS

Q.W.: investigation, methodology, and writing—original draft. X.Z.: investigation and methodology. H.S.: investigation. M.Z.: methodology. Z.L.: conceptualization and supervision. T.W.: conceptualization, supervision, writing—review and editing, and funding acquisition.

COMPETING INTERESTS

The authors declare no competing interests.

ADDITIONAL INFORMATION

Correspondence and requests for materials should be addressed to Tangqing Wu.

Reprints and permission information is available at <http://www.nature.com/reprints>

Publisher's note Springer Nature remains neutral with regard to jurisdictional claims in published maps and institutional affiliations.



Open Access This article is licensed under a Creative Commons Attribution 4.0 International License, which permits use, sharing, adaptation, distribution and reproduction in any medium or format, as long as you give appropriate credit to the original author(s) and the source, provide a link to the Creative Commons license, and indicate if changes were made. The images or other third party material in this article are included in the article's Creative Commons license, unless indicated otherwise in a credit line to the material. If material is not included in the article's Creative Commons license and your intended use is not permitted by statutory regulation or exceeds the permitted use, you will need to obtain permission directly from the copyright holder. To view a copy of this license, visit <http://creativecommons.org/licenses/by/4.0/>.

© The Author(s) 2022